Article type: Full Paper Origin of ferroelectric phase in undoped HfO2 films deposited by sputtering

Preprint · May 2019

DOI: 10.13140/RG.2.2.28236.05767

DOI: 10.1002/

Article type: Full Paper

Origin of ferroelectric phase in undoped HfO_2 films deposited by sputtering

T. Mittmann[1], M. Materano[1], P. D. Lomenzo[1], M. H. Park[1,2], I. Stolichnov[3], M. Cavalieri[3], C. Zhou[4], J. L. Jones[4], T. Szyjka[5], M. Müller[5,6], A. Kersch[7], T. Mikolajick[1,8] and U. Schroeder[1]*

[1] *NaMLab gGmbH, Noethnitzer Str. 64, 01187 Dresden, Germany, terence.mittmann@namlab.com*
[2] *School of Materials Science and Engineering, Pusan National University, 2, Busandaehak-ro 63 beon-gil, Geumjeong-gu, Busan 46241, Republic of Korea*
[3] *Nanoelectronic Devices Laboratory, Ecole Polytechnique Fédérale de Lausanne (EPFL), Lausanne 1015, Switzerland*
[4] *Department of Materials Science and Engineering, North Carolina State University, Raleigh, USA*
[5] *Forschungszentrum Jülich GmbH, Peter Grünberg Institut (PGI-6), 52425 Jülich, Germany*
[6] *Faculty of Physics, TU Dortmund, 44221 Dortmund, Germany*
[7] *Department of Applied Sciences and Mechatronics, Munich University of Applied Sciences, 80335 Munich, Germany*
[8] *Chair of Nanoelectronic Materials, TU Dresden, 01062 Dresden, Germany*

Keywords: Hafnia, Ferroelectricity, Sputtering, Oxygen vacancies, orthorhombic phase

Thin film metal-insulator-metal capacitors with undoped HfO_2 as the insulator are fabricated by sputtering from ceramic targets and subsequently annealed. The influence of film thickness and anneal temperature is characterized by electrical and structural methods. After annealing, the films show distinct ferroelectric properties. Grazing incidence x-ray diffraction measurements reveal a dominant ferroelectric orthorhombic phase for thicknesses in the 10-50 nm range and a negligible non-ferroelectric monoclinic phase fraction. Sputtering HfO_2 with additional oxygen during the deposition decreases the remanent polarization. Overall, the impact of oxygen vacancies and interstitials in the HfO_2 film during deposition and anneal is correlated to the phase formation process.

1. Introduction

Since Böscke et al. reported ferroelectricity (FE) in thin atomic layer deposited (ALD) Si doped HfO_2 films [1], many other dopants such as Al, Gd, La, Sr, Y, and Zr are reported to induce ferroelectric properties in HfO_2. [2–7] Whereas bulk HfO_2 crystallizes in a monoclinic phase (m-phase, space group: $P2_1/c$), it is believed that the ferroelectricity in doped HfO_2 results from the formation of a non-centrosymmetric $Pca2_1$ orthorhombic phase (o-phase). [1–7] For increasing doping concentrations, ALD HfO_2 films undergo a phase transition from a non-ferroelectric m-phase to ferroelectric orthorhombic phase and for higher concentrations to the tetragonal phase (t-phase, space group: $\underline{P}4_2/nmc$) if the dopants are smaller than Hf like Si and Al, or to the cubic phase if the dopants are larger than Hf like Gd, La, Sr, and Y. [8] Besides the influence of doping, four other factors are known to promote the stabilization of the ferroelectric phase: surface or interface/grain boundary energy, film stress, and the presence of oxygen vacancies. [9–13] Oxygen vacancies and the related defect states play an important role in the so-called wake up effect. [14] Wake up describes the increase of the remanent polarization during electrical field cycling with opening of an initially pinched polarization-voltage hysteresis. [11] In $Hf_{1-x}Zr_xO_2$ films, Materlik *et al.* suggested that the bulk and surface free energy of the o-phase is located between those of the m-phase and t-phase. As a result, the o-phase is stabilized in a specific film thickness and grain size region. This suggestion matches well with many experimental results on the effect of film thickness and/or grain size for the ferroelectric phase formation. [9,10,15] Experimentally, a ferroelectric phase could be formed in undoped HfO_2 by tuning the grain size which can be controlled by thermal treatment and film thickness. [13,16] Polakowski *et al.* and Kim *et al.*.[17,18] obtained the ferroelectric phase at reduced ALD deposition temperatures and for decreased film thicknesses below 10 nm. Both methods reduced the grain size and stabilized the o-phase in undoped HfO_2. Besides the aforementioned thermodynamic

mechanisms, Park et al. recently suggested that the metastable orthorhombic phase formation can be attributed to the kinetic suppression of the formation of the monoclinic phase due to the rather high kinetic activation barrier for the tetragonal/orthorhombic to monoclinic phase transformation. [19]

Ferroelectric HfO_2-based thin films could be reproducibly deposited using various deposition techniques such as ALD, chemical vapor deposition (CVD), chemical solution deposition (CSD), pulsed laser deposition (PLD), and sputtering (PVD). [20] Among these techniques, the most intensively studied deposition technique is ALD. For the case of ALD, however, there are less deposition parameters which can be controlled, since ALD is based on a self-limiting mechanism with chemical reactions between a metal precursor, oxygen source, and substrate or previously deposited film. Typical parameters are only deposition temperature and precursor/purge pulse times. On the other hand, for PVD, various factors such as sputtering power, sputter atmosphere, and deposition temperature can be easily controlled, suggesting that PVD is an attractive deposition technique to study root causes of the unexpected ferroelectric phase formation in HfO_2-based thin films. Contaminants within the film are mainly determined by the target quality. The first report of sputtered ferroelectric HfO_2-based films used Y doping and later extensive studies with other dopants followed. [21–23] These studies showed improved ferroelectricity in HfO_2 by co-sputtering from oxide targets, but also undoped sputtered HfO_2 films showed signs of ferroelectricity.

In this study, RF sputtering as a PVD method is used to fabricate undoped HfO_2 thin films. The fabricated PVD films are compared to ALD deposited films as reported in literature to gain deeper insight into the mechanisms involved in the formation of the ferroelectric phase in undoped HfO_2 films. [17,24] For ALD HfO_2 films, carbon from the residual precursor ligands will be present as a significant source of contamination, whereas in PVD HfO_2 films, only a low amount of processing gases were reported. [18] In addition, the possibility to grow the films

at room temperature together with higher deposition rates changes the deposition kinetics when sputtering is used compared to ALD. The benefit of characterizing the ferroelectric properties in undoped HfO_2 films is that the number of factors influencing the formation of the ferroelectric HfO_2 phase are reduced. With the effect of doping removed, studies can focus on the impact of the remaining factors responsible for the formation of the ferroelectric phase. In particular, the influence of oxygen content in thin HfO_2 films on the phase composition and the according ferroelectric properties will be investigated. Comparable studies were performed for HfO_2 powders, which showed similar trends. [25–27]

2. Experimental

Metal-insulator-metal (MIM) capacitor structures were fabricated on silicon substrates for electrical and structural characterization. The MIM capacitors were deposited in a BESTEC ultra-high vacuum (UHV) sputter cluster equipped with three chambers. Using one chamber for metal deposition and two for dielectrics, it is possible to build the film stack without breaking vacuum. TiN top and bottom electrodes were deposited at room temperature from a 3 inch Ti target in 20 sccm Ar and 4 sccm N_2 flow at $1.2 \cdot 10^{-3}$ mbar. A 3 inch ceramic HfO_2 target with 99.9 % purity bonded on a copper back plate was used for the deposition of HfO_2 films with various thicknesses between 8 nm and 40 nm using 20 sccm Ar flow at $1.2 \cdot 10^{-3}$ mbar. The sputter power was kept constant at 100 W to lower the potential effect of a changed deposition rate and particle energies and a 1000 V DC bias was applied. For changing the oxygen content in the film additional oxygen flux was let into the vacuum chamber at the substrate. A subsequent thermal treatment is necessary to fully crystallize the deposited HfO_2 films and to obtain ferroelectricity. Therefore, a rapid thermal processing (RTP) step follows the MIM fabrication to crystallize the HfO_2 film. Annealing was performed at different temperatures under N_2-atmosphere. Anneals lasted 20 s for temperatures ranging from 500 to 800 °C and 1 s

at 1000 °C. For electrical characterization, a 10 nm Ti adhesion layer and 50 nm Pt circular contacts were deposited using e-beam evaporation through a shadow mask on top of the TiN layer. The TiN in between the Ti/Pt dots was etched with an SC1 solution of 50:2:1 H_2O:H_2O_2:NH_4OH for 5 min at 50 °C to form the capacitor geometry.

Thickness and density of the films were determined by X-ray reflectivity (XRR) on a Bruker D8 Discover XRD system with a Cu K_α source. The crystal structure was investigated by grazing-angle incidence X-ray diffraction (GIXRD) on the same D8 Discover system. Images of the grains were taken using a Zeiss Leo 1560 scanning electron microscope (SEM). For chemical analysis, hard X-ray photoelectron spectroscopy (HAXPES) was performed at the P22 beamline of the Petra III storage ring at DESY (Hamburg). For the bulk-sensitive analysis, photoelectrons were excited using 5978.35 eV photon energy at 10 ° incident angle and detected in normal emission geometry. The energy resolution was set to 30 meV and the energy scale was calibrated to a Au reference. Polarization and local hysteretic piezo response in the nanometer scale have been detected via piezoresponse force microscopy (PFM) using an Asylum Research Cypher atomic force microscope in the off-resonance mode as described elsewhere.[28] The polarization hysteresis (performed with an excitation frequency at 10 kHz) and fatigue measurements (using an excitation frequency of 100 kHz) were performed on an aixACCT TF Analyzer 3000. The maximum electric field was about 3 MV/cm.

3. Discussion

The capacitors described above were investigated regarding their ferroelectric properties. **Figure 1** shows the switchable polarization $2P_r$ of various films with different HfO_2 thicknesses from 8 nm to 30 nm and annealed at different temperatures from 500 °C to 1000 °C. It can be seen that 500 °C and 600 °C anneals are not sufficient to induce ferroelectricity in any of the

examined thicknesses. For higher anneal temperatures, films show a stable remanent polarization. The highest $2P_r$ of 20.2 µC/cm² nearly matches the results reported for ALD deposited films at an electrical field of 4 MV/cm (see **Figure 3**). [17] The impact of the anneal temperature on the remanent polarization changes with film thickness. From 8 nm to 20 nm, $2P_r$ increases with increasing temperature. In contrast, the 800 °C anneal seems to be the optimal anneal temperature for thicker films. This is caused by a lowered crystallization temperature and a preferred transformation to the monoclinic phase for thicker films as will be discussed later. [13,29] Additionally, the 800 °C annealed samples exhibit the most stable polarization at different thicknesses in the pristine state and after wake-up cycling. However, samples annealed at this temperature possess a much stronger polarization increase with electrical field cycling than the 1000 °C annealed films (see **Figure 2**). The higher anneal temperature causes a more homogeneous distribution of defects and ferroelectric domains in the film. [11] This effect increases the initial number of switchable domains within the ferroelectric film and thus the pristine remanent polarization is increasing. In previous studies a similar effect could be shown for ALD deposited $Hf_{0.5}Zr_{0.5}O_2$ thin films. [16]

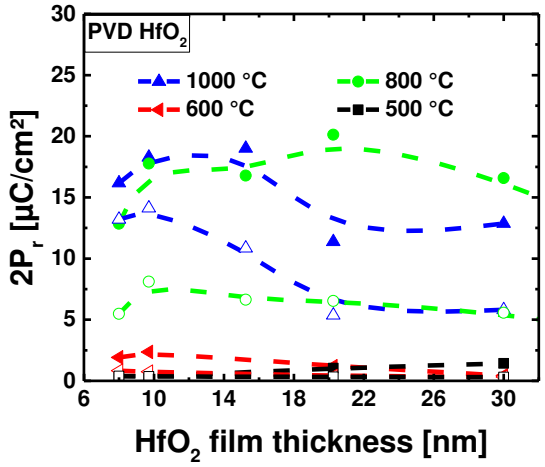

Figure 2: Double remanent polarization $2P_r$ for sputtered undoped HfO_2 films as a function of film thicknesses and anneal

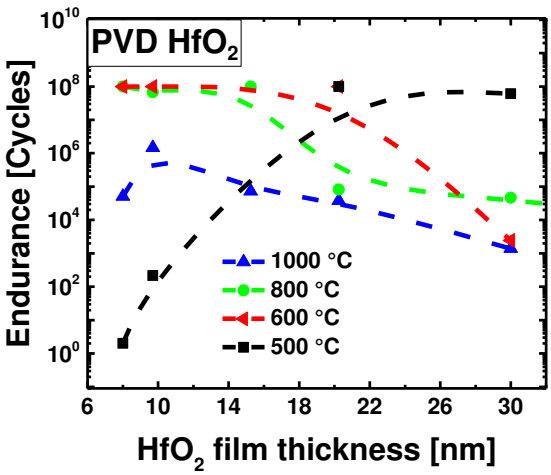

Figure 1: Number of cycles to breakdown of HfO_2 films as a function of film thickness and anneal temperature. Cycling was stopped after 10^8 electrical field cycles were reached.

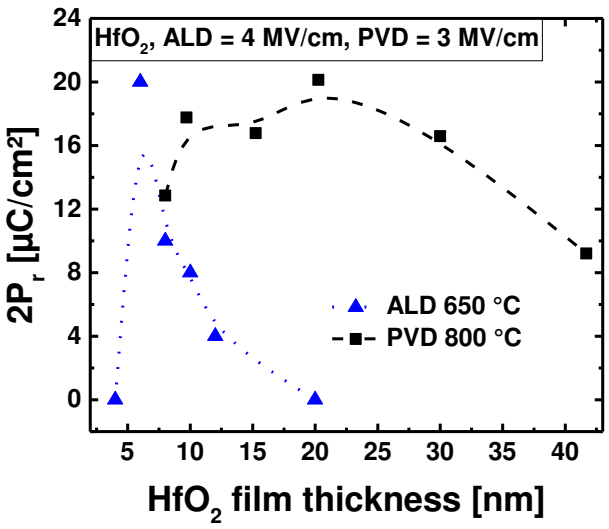

Figure 3: Thickness dependence of the double remanent polarization $2P_r$ of ALD and PVD deposited HfO_2 based MIM capacitors. The broken lines are guides to the eyes.

In Figure 2 the number of field cycles to breakdown (endurance) for different film thicknesses and annealing temperatures is shown. To keep the measurement time in a reasonable range, the maximum number of applied cycles was 10^8. Therefore, the endurance of samples reaching 10^8 cycles is equal to or greater than 10^8. The number of electric field cycles before the dielectric breakdown decreases for increasing anneal temperature from 600 °C to 1000 °C and with increasing film thickness. Higher temperatures not only result in a more homogenous defect distribution, but also in an increased defect concentration, diffusion of defects, and migration of titanium/nitrogen ions from the electrode along grain boundaries into the film. [30] The larger defect concentration also decreases the number of cycles to breakdown for increasing anneal temperature. In addition, the higher polarization of films annealed at temperatures above 800°C leads to a higher charge injection and increased defect generation.[31,32] Samples annealed at 500 °C show an opposite behavior because of the changed crystalline properties. As determined by GIXRD, the 10 nm thick sample is crystalline for anneals at 600 °C and above (see **Figure 4**) and only an amorphous background signal is detected for as-deposited samples up to 500°C anneal temperatures. Samples have a relatively high endurance that drops for lower anneal temperatures than 600 °C where films are mainly amorphous. Overall, the crystallization temperature of PVD deposited

HfO_2 is raised relative to ALD samples as explained later in the text. The identified thickness dependent polarization of the sputtered HfO_2 films is compared with those of published ALD films in Figure 3. [17] The ferroelectricity in sputtered HfO_2 is retained up to much larger thicknesses for PVD relative to ALD films that exhibit ferroelectricity only in undoped HfO_2 films thinner than 12 nm. Polakowski et al. assumed that the decreased grain size for films with a thickness lower than 10 nm stabilizes the ferroelectric phase. [17] Additionally from DFT simulations and former experiments, it is known that an increase in the grain size in thicker films destabilizes the orthorhombic and stabilizes the monoclinic phase as a consequence of an increase of the surface energy to bulk energy ratio. [15] Accordingly, other factors than surface and grain boundary energy play a more prominent role in the stabilization of the ferroelectric phase in undoped HfO_2 deposited by PVD.

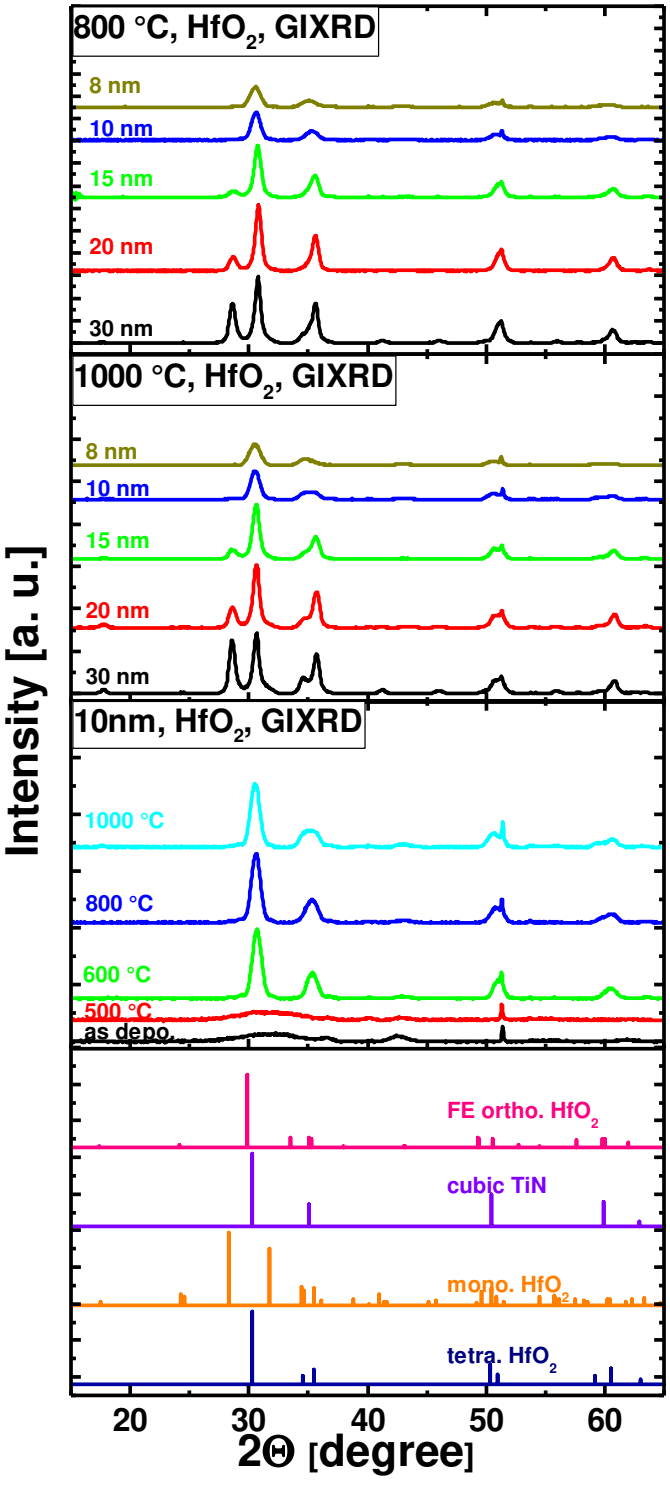

Figure 4: GIXRD patterns of undoped sputtered HfO_2 for different thicknesses from 8 to 30 nm and for 10nm thick films with different anneal temperatures

To prove that the hysteretic behavior of HfO_2 films shown above has a ferroelectric origin, the individual nanometer-scale domains were monitored by piezo response force microscopy (PFM) on a 10 nm thick HfO_2 film annealed at 1000 °C. PFM maps of the amplitude and phase of local piezoelectric response have been collected on the HfO_2 capacitors through the TiN/Pt 30nm top electrode (**Figure 5 a-f**). The measurements have been carried out using the off-resonance PFM technique with the ac signal of 0.5V/91 kHz.[28] The nanometer-scale switching data in Fig. 4 reveals a switching asymmetry: the tip bias of +3V results in a complete switching (homogeneous phase map) while the opposite bias produces only partial switching with about 30% of non-reversed domains. The PFM maps of this partially switched state clearly show the domain structure where the opposite domains are signaled by bright color (Figure 5 a-c: phase

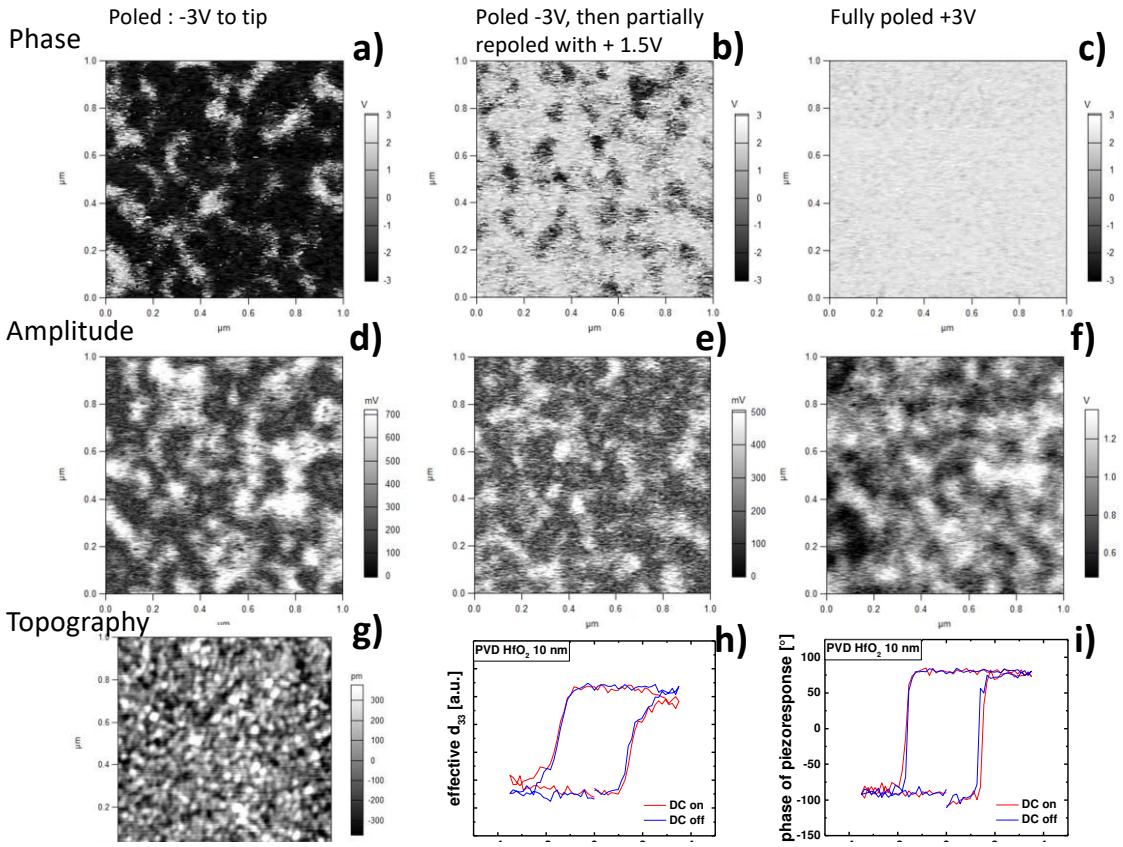

Figure 5 a)-i): PFM image (phase/amplitude/topography) of MIM capacitor with 10 nm HfO_2, measured on a Pt/TiN top electrode. a) and d): poled with -3V on tip; b) and e) poled at -3V, then partially repoled with + 1.5V; c) and f) fully poled with +3V on tip. The domains are completely switchable in the positive direction. PFM images extracted from a MIM capacitor with 10 nm HfO_2 and measured on a TiN electrode without precycling. Domains do not back switch completely after application of -3 V to the top electrode with 26 % white regions. h) Loop of effective d_{33}. i) Phase change of 180° on one spot on the surface.

map) and outlined by dark zones at the boundaries (amplitude maps). These PFM results which show partial switching are consistent with the macroscopic switching data (Figure 1) where the initial switching polarization is 22% lower than the value achieved after the wake-up procedure. The ferroelectricity of the capacitors used in this study is further confirmed by local hysteresis loops of the transverse piezoelectric coefficient d_{33} (Figure 5 h,i). The sharp 180° phase change during switching and the saturating voltage dependence of d_{33} loops attest to the true ferroelectric origin of the observed hysteretic behavior.

With the confirmation of ferroelectric switching shown by the PFM results, the crystal structure is examined by GIXRD to identify the nonpolar orthorhombic phase which is the origin of ferroelectricity in HfO_2 as explained above. The investigated HfO_2 thin films of various thicknesses annealed at 800 °C and 1000 °C have polycrystalline structures and Figure 4 evidences that the orthorhombic and/or tetragonal phase is the most prominent phase. Films with film thicknesses above 15 nm have an increasing monoclinic phase fraction. This effect was also investigated for ALD deposited HfO_2.[17] For ALD films, a significant increase of the m-phase from 15 % to 60 % for increasing film thickness from 6 nm to 20 nm occurred, which was accompanied by a destabilization of the o-phase. The increase of the m-phase fraction is weaker in PVD deposited HfO_2 films.[17] To distinguish between the o- and t-phase, a Rietveld refinement was performed identifying a predominant o-phase. The higher monoclinic phase fraction in 20 and 30 nm thick films annealed at 1000 °C causes the decrease in remanent polarization. Films annealed at 600 °C exhibit a strong o(111)/t(011) peak at 30.5° but only a small remanent polarization. [33] The MIM capacitors annealed at 600 °C had a strongly pinched hysteresis loop which slightly opened up during field cycling. Accordingly, a dominant t-phase fraction can be assumed.

In ALD manufactured HfO_2 films, it could be observed that the initial phase of formed nano-crystallites during the film deposition strongly impacts the later polymorphism.[15,34] The diffuse

GIXRD pattern of the as-deposited sputtered 10 nm HfO_2 shown in the bottom of Figure 4 indicates a mainly amorphous structure with 1 nanometer crystallites. In contrast to ALD deposited films, the GIXRD pattern after annealing at 500 °C for 20 s still indicates a mostly amorphous film with discontinuous nano-crystallites. One possible conclusion from this result would be a higher nucleation energy in PVD compared to ALD films. Since ALD films are deposited by higher deposition temperatures compared to the PVD films, the higher thermal energy lowers the subsequent activation energy for nucleation causing crystallization to proceed with less thermal energy input during the annealing process. In addition, a possible difference in the nucleation energy could be caused by a lower number of impurities observed in PVD films because of direct sputtering from nominally HfO_2 targets. In particular, ALD often has a higher carbon incorporation owing to the organic based precursors. For the comparison of the carbon content of ALD and PVD manufactured films, time-of-flight secondary ion mass spectrometry (ToF-SIMS) is used in this study. Independent of the annealing temperature, PVD-deposited films contain ten times lower carbon concentration (~0.1 at%) compared to ALD-deposited films of (~1 at%) (Figure SI 5). Larger grain sizes of 20 nm in PVD films, compared to grain sizes of 8 nm observed in ALD films (Figure SI 4), support this assumption, since a higher carbon concentration would lead to a larger number of grains as well as a suppressed grain growth.[16,35] In addition, different concentrations of oxygen in ALD vs. PVD films as discussed in the later part of the text could impact the crystallization behavior.

It is already known from ALD deposited undoped HfO_2 films that oxygen vacancies can be a driving force or at least an important factor in the stabilization of the metastable ferroelectric

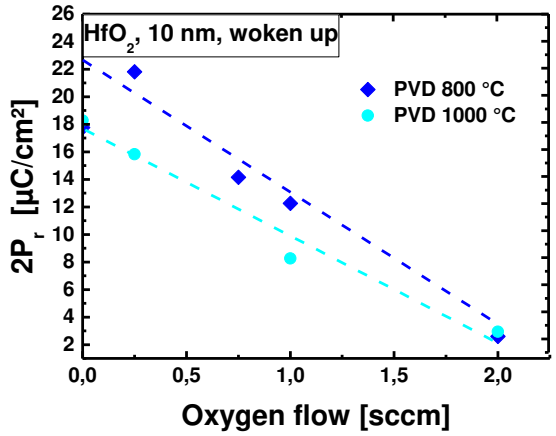

Figure 6 Double remanent polarization $2P_r$ as a function of the oxygen flow during PVD deposition of HfO_2 films

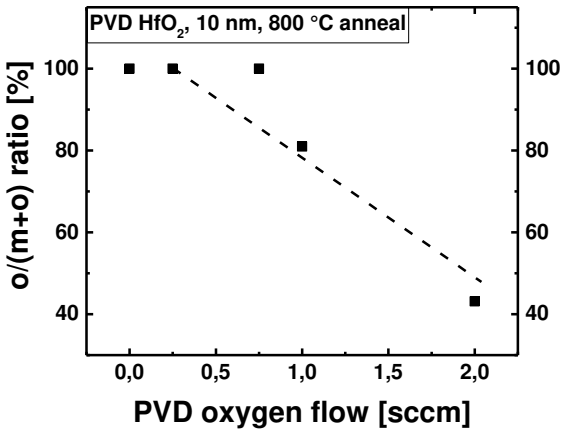

Figure 7: o/m-ratio calculated from peak areas of GIXRD pattern of sputtered HfO_2 films with different oxygen ambient during deposition

orthorhombic phase. [24,36] Due to film deposition by sputtering from an oxide target, an unbalanced sputtering and deposition of Hf and O can occur which results in sub-stoichiometric films with a higher amount of oxygen vacancies. To check this assumption, HfO_2 films with an additional oxygen flow from 0.25 to 2 sccm at the substrate were deposited.

Figure 6 shows the remanent polarization $2P_r$ as a function of the oxygen flow at the substrate during HfO_2 deposition. It can be seen that a higher oxygen flow during deposition decreases the remanent polarization. This is correlated with an increase of the monoclinic phase portion and a decrease of the orthorhombic phase as can be seen in the o/(o+m)-ratio in **Figure 7**. The o/(o+m)-ratio is calculated by using the peak areas of the o(111), m(-111), and m(111) diffraction peaks at 30.5°, 28.5°, and 31.6° as described for the m-phase fraction in [6]. **Figure 9** shows XRD spectra of annealed 10 nm thick HfO_2 films sputtered with different oxygen partial pressures during deposition. Less oxygen during deposition may lead to more oxygen vacancies in the HfO_2 films. Similar to the discussion above, the different oxygen concentrations in HfO_2 are leading to different nucleation behaviors which impact the formation of the crystal phase and according polarization values. Comparing GIXRD results of as deposited PVD HfO_2 films

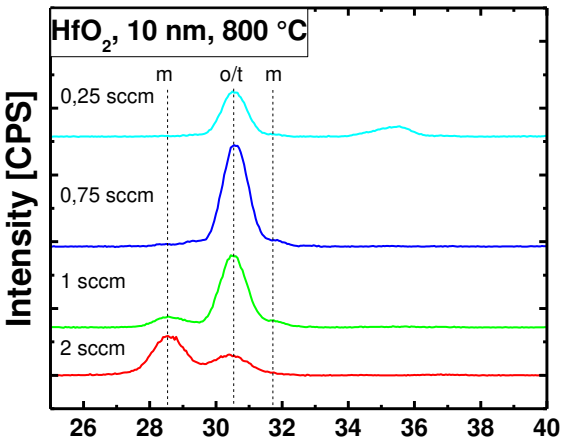

Figure 8: GIXRD patterns of 10 nm HfO_2 films sputtered with different oxygen flows after 800 °C anneal.

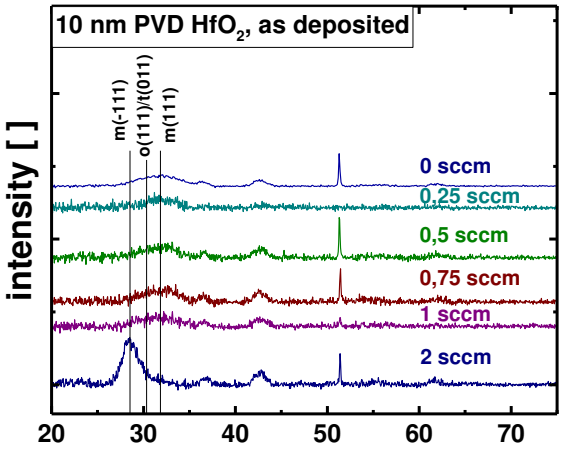

Figure 9: GIXRD patterns of as deposited 10 nm thick sputtered HfO_2 films deposited with different oxygen partial pressure during the sputtering process

(**Figure 8**) and the case after 800 °C anneal (Figure 9), nuclei of certain phases are already present after deposition that determine the later predominant phase of the film. HfO_2 films with low O_2 flow show broad o/m-phase diffraction peaks as expected for mainly amorphous films in contrast to m-phase nuclei for the highest O_2 flow. In parallel, the peak width of the m-phase peak is reduced, indicating larger m-phase grain nuclei for higher O_2 flow. The crystallite size in the as-sputtered films, determined by Scherrer's equation, remains roughly constant at about 1 nm until an O_2 flow of 2 sccm is used which causes larger 4 nm monoclinic crystallites to nucleate (Figure SI 10). Similar to these results, ALD based HfO_2 films also exhibit an improvement in ferroelectricity for lower oxygen content during deposition[24] caused by shorter O_3 precursor pulse times, although the predominant phases are shown only after high temperature annealing and the nucleating phase is not clear. To prove the assumption of different oxygen vacancies levels, samples with 2 sccm additional oxygen flow and without oxygen were examined by HAXPES (**Figure 10**). In the layers without additional oxygen a shift of the Hf 4f and the O1s peaks towards higher binding energy was observed, while the Ti 2p levels remain unaffected for both samples (not shown here). With regard to the literature [37,38] this peak shift is related to a downward band bending caused by an increasing amount of oxygen vacancies at the HfO_2/Ti electrode interface. Here one has to take into account that the O1s peak can be superimposed with other peaks and the Hf4f peaks are separated from other

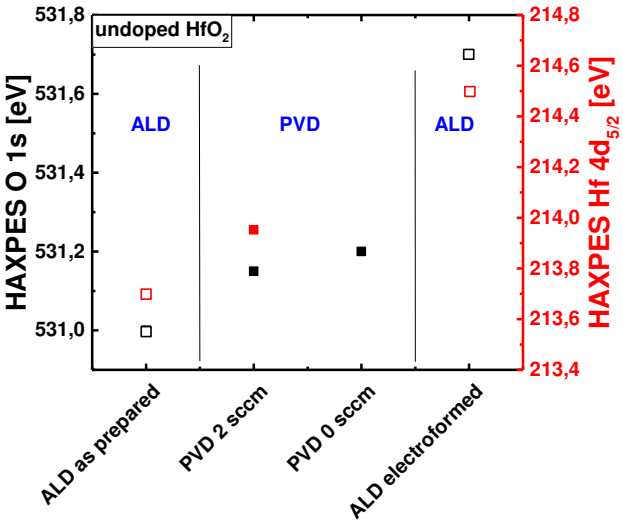

Figure 10: Change in the binding energies of the O 1s and Hf 4d 5/2 peak for ALD and PVD deposited films. Closed symbols – this work; open symbols Sowinska et al. [38]

features. Both peaks are in between the peak positions determined by Sowinska et al. for ALD as-deposited HfO_2 films and after forming a low resistive state with high amount of oxygen vacancies.[38] Since no additional interstitial O feature at 528 eV is observed in the O 1s peak for PVD HfO_2 films with additional oxygen flow, this interstitial oxygen amount is expected to be low for crystalline HfO_2 (See Figure SI 6 and Figure SI 7) [39]. For amorphous HfO_2 (not shown), interstitial O is difficult to be detected and, accordingly, it is expected that no feature is present. Overall, this confirms that the number of oxygen vacancies in the HfO_2 can be influenced by additional oxygen flow during sputter deposition.

Independent of the deposition method, nucleation can be described by the Ostwald's rule, which states that not the most but the least stable polymorph crystallizes first. [40] Following the free energy as calculated by DFT (SI figure 9), nucleation would start in the phase with the highest free energy (cubic phase) and transform to phase with lower free energy depending on the grain size (cubic to tetragonal to orthorhombic to monoclinic transition). This approach follows the same explanation path as discussed by Materlik et al. [41] using a surface/interface model. Again, a grain size dependent phase formation is expected which can be experimentally shown in temperature dependent GIXRD measurements (see SI Fig. 8). Since a high activation barrier is reported between the o- and m-phase as described by Park et al., a metastable ferroelectric o-phase can be formed under certain process conditions (e.g. thermal budget). The amount of oxygen within the HfO_2 layer can impact the nucleation and grain growth behavior.

As mentioned above for PVD deposited films, oxygen deficient HfO_2 films are almost amorphous with some small nuclei within the layer likely positioned at defects (see **Figure 11**). For heterogeneous nucleation these defect sites are likely at film interfaces. During polymorphic crystallization at 800°C, the amorphous and crystalline phase are of the same composition and the oxygen content in the layer is kept. The nucleation is following the above mentioned grain size dependent phase formation. For smaller grains the higher surface and interface energy causes the formation of the t-phase at 800°C, since a high activation barrier is inhibiting a phase transformation to the m-phase. During cool down the t-phase is transformed to the o-phase below Curie temperature.

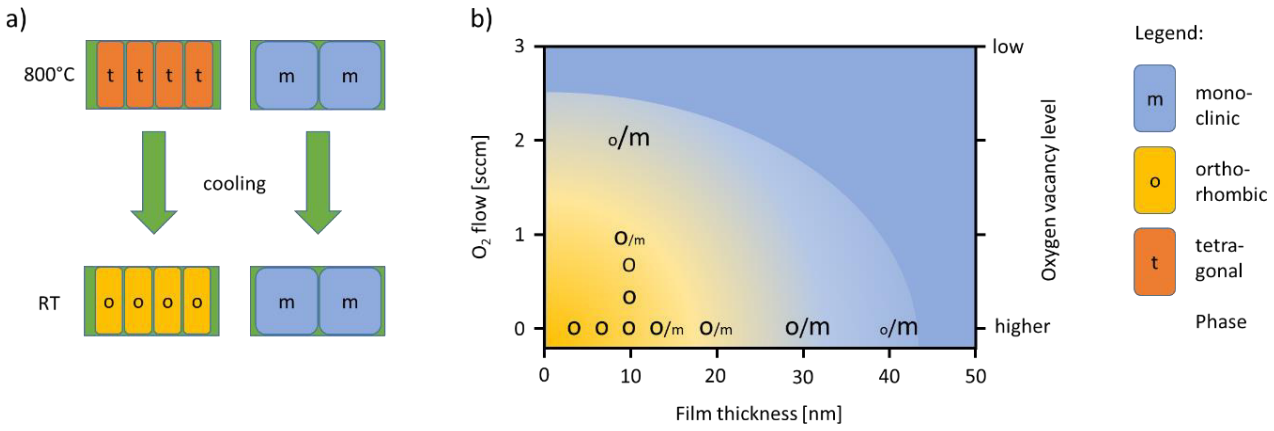

Figure 11 a) Phase formation during cooling: depending on the grain size a different phase is formed b) The grain size can be impacted by the layer thickness or the defect/oxygen vacancy level in the film. [42]

In contrast for oxygen rich PVD deposited HfO_2 films, more oxygen is available leading to a lower energy required for nucleation. Hence, a lower incubation time is reducing the crystallization temperature and larger nuclei are already present in the as-deposited HfO_2 at room temperature (figure SI 10). According to DFT calculations the t-phase formation is suppressed for higher oxygen concentrations in HfO_2 (figure SI 9) and m-phase nuclei are formed. These m-phase nuclei are determining the dominate phase of the crystallized layer during 800°C anneal.

4. Conclusion

In conclusion, sputtering HfO_2 from ceramic HfO_2 targets is an effective way to produce stable ferroelectric films over a wide thickness range with high remanent polarization $2P_r$ of 18 - 20 µC/cm² without using additional doping. Ferroelectric properties are confirmed on macroscopic capacitor structures and by PFM on the nanometer scale. The results indicate that the defect structure in thin films is extremely important for the stabilization of the orthorhombic phase. The concentration of oxygen within the HfO_2 film can be directly or indirectly responsible for the stabilization of the orthorhombic phase. With increasing oxygen flow during the sputter deposition of undoped HfO_2, it was possible to vary the amount of oxygen vacancies incorporated in the HfO_2 films as confirmed by HAXPES. The concentration of oxygen determines the nucleating phase of nano-crystallites in the as deposited films, which impacts the later phase transitions during annealing and cooling to room temperature in the HfO_2 films. Here, the ferroelectric orthorhombic phase is preferred in oxygen deficient layers, whereas oxygen rich films could initiate larger monoclinic grains. The observation of a very low monoclinic phase fraction in combination with high remanent polarization values make undoped sputtered HfO_2 an excellent candidate for applications where doping needs to be avoided. Moreover, the obtained results help to further clarify the factors influencing the stabilization of the metastable orthorhombic phase in hafnium thin films.

Acknowledgements

T.S., M.Mü., I.S., M.C. received funding from the European Union's Horizon 2020 research and innovation program under grant agreement No 780302 (project 3εFerro). M.H.P. was supported by Humboldt postdoctoral fellowship from Alexander von Humboldt Foundation and later by the Basic Science Research Program through an NRF (National Research Foundation of Korea) grant funded by the Ministry of Education (NRF-2018R1C1B5086580). P.D.L is funded by the German Ministry of Economic Affairs and Energy (BMWi) project (16IPCEI310). This work was performed in part at the Analytical Instrumentation Facility (AIF) at North Carolina State Univ., which is supported by the State of North Carolina and the National Science Foundation (Award No. ECCS-1542015). The AIF is a member of the North Carolina Research Triangle Nanotechnology Network (RTNN), a site in the National Nanotechnology Coordinated Infrastructure (NNCI).

Received:

Revised:

Published online:

[1] T. S. Böscke, J. Müller, D. Bräuhaus, U. Schröder, U. Böttger, *Appl. Phys. Lett.* **2011**, *99*, 102903.

[2] S. Mueller, J. Mueller, A. Singh, S. Riedel, J. Sundqvist, U. Schroeder, T. Mikolajick, *Adv. Funct. Mater.* **2012**, *22*, 2412.

[3] S. Mueller, C. Adelmann, A. Singh, S. Van Elshocht, U. Schroeder, T. Mikolajick, *ECS J. Solid State Sci. Technol.* **2012**, *1*, N123.

[4] U. Schroeder, C. Richter, M. H. Park, T. Schenk, M. Pešić, M. Hoffmann, F. P. G. Fengler, D. Pohl, B. Rellinghaus, C. Zhou, C.-C. Chung, J. L. Jones, T. Mikolajick, *Inorg. Chem.* **2018**, *57*, 2752.

[5] T. Schenk, S. Mueller, U. Schroeder, R. Materlik, A. Kersch, M. Popovici, C. Adelmann, S. Van Elshocht, T. Mikolajick, In *2013 Proceedings of the European Solid-State Device Research Conference (ESSDERC)*; IEEE: Bucharest, 2013; pp. 260–263.

[6] J. Müller, U. Schröder, T. S. Böscke, I. Müller, U. Böttger, L. Wilde, J. Sundqvist, M. Lemberger, P. Kücher, T. Mikolajick, L. Frey, *J. Appl. Phys.* **2011**, *110*, 114113.

[7] J. Müller, T. S. Böscke, U. Schröder, S. Mueller, D. Bräuhaus, U. Böttger, L. Frey, T. Mikolajick, *Nano Lett.* **2012**, *12*, 4318.

[8] U. Schroeder, E. Yurchuk, J. Müller, D. Martin, T. Schenk, P. Polakowski, C. Adelmann, M. I. Popovici, S. V. Kalinin, T. Mikolajick, *Jpn. J. Appl. Phys.* **2014**, *53*, 08LE02.

[9] H. J. Kim, M. H. Park, Y. J. Kim, Y. H. Lee, W. Jeon, T. Gwon, T. Moon, K. D. Kim, C. S. Hwang, *Appl. Phys. Lett.* **2014**, *105*, 192903.

[10] R. Materlik, C. Künneth, A. Kersch, *J. Appl. Phys.* **2015**, *117*, 134109.

[11] M. Pešić, F. P. G. Fengler, L. Larcher, A. Padovani, T. Schenk, E. D. Grimley, X. Sang, J. M. LeBeau, S. Slesazeck, U. Schroeder, T. Mikolajick, *Adv. Funct. Mater.* **2016**, *26*, 4601.

[12] R. Batra, T. D. Huan, G. A. Rossetti, R. Ramprasad, *Chem. Mater.* **2017**, *29*, 9102.

[13] M. Hyuk Park, H. Joon Kim, Y. Jin Kim, W. Lee, T. Moon, C. Seong Hwang, *Appl. Phys. Lett.* **2013**, *102*, 242905.

[14] M. Hoffmann, U. Schroeder, T. Schenk, T. Shimizu, H. Funakubo, O. Sakata, D. Pohl, M. Drescher, C. Adelmann, R. Materlik, A. Kersch, T. Mikolajick, *J. Appl. Phys.* **2015**, *118*, 072006.

[15] M. H. Park, Y. H. Lee, H. J. Kim, T. Schenk, W. Lee, K. D. Kim, F. P. G. Fengler, T. Mikolajick, U. Schroeder, C. S. Hwang, *Nanoscale* **2017**, *9*, 9973.

[16] T. Mittmann, F. P. G. Fengler, C. Richter, M. H. Park, T. Mikolajick, U. Schroeder, *Microelectron. Eng.* **2017**, *178*, 48.

[17] P. Polakowski, J. Müller, *Appl. Phys. Lett.* **2015**, *106*, 232905.

[18] K. D. Kim, M. H. Park, H. J. Kim, Y. J. Kim, T. Moon, Y. H. Lee, S. D. Hyun, T. Gwon, C. S. Hwang, *J. Mater. Chem. C* **2016**, *4*, 6864.

[19] M. H. Park, Y. H. Lee, H. J. Kim, Y. J. Kim, T. Moon, K. D. Kim, S. D. Hyun, T. Mikolajick, U. Schroeder, C. S. Hwang, *Nanoscale* **2018**, *10*, 716.

[20] U. Schroeder, C. S. Hwang, H. Funakubo, *Ferroelectricity in doped hafnium oxide: materials, properties and devices*; 1st ed.; Elsevier, 2019.

[21] T. Olsen, U. Schröder, S. Müller, A. Krause, D. Martin, A. Singh, J. Müller, M. Geidel, T. Mikolajick, *Appl. Phys. Lett.* **2012**, *101*, 082905.

[22] L. Xu, S. Shibayama, K. Izukashi, T. Nishimura, T. Yajima, S. Migita, A. Toriumi, In *2016 IEEE International Electron Devices Meeting (IEDM)*; IEEE: San Francisco, CA, USA, 2016; pp. 25.2.1-25.2.4.

[23] L. Xu, T. Nishimura, S. Shibayama, T. Yajima, S. Migita, A. Toriumi, *J. Appl. Phys.* **2017**, *122*, 124104.

[24] A. Pal, V. K. Narasimhan, S. Weeks, K. Littau, D. Pramanik, T. Chiang, *Appl. Phys. Lett.* **2017**, *110*, 022903.

[25] P. Rauwel, E. Rauwel, C. Persson, M. F. Sunding, A. Galeckas, *J. Appl. Phys.* **2012**, *112*, 104107.

[26] M. Forker, P. de la Presa, W. Hoffbauer, S. Schlabach, M. Bruns, D. V. Szabó, *Phys. Rev. B* **2008**, *77*.

[27] C.-H. Lu, J. M. Raitano, S. Khalid, L. Zhang, S.-W. Chan, *J. Appl. Phys.* **2008**, *103*, 124303.

[28] I. Stolichnov, M. Cavalieri, E. Colla, T. Schenk, T. Mittmann, T. Mikolajick, U. Schroeder, A. M. Ionescu, *ACS Appl. Mater. Interfaces* **2018**, *10*, 30514.

[29] E. Yurchuk, J. Müller, S. Knebel, J. Sundqvist, A. P. Graham, T. Melde, U. Schröder, T. Mikolajick, *Thin Solid Films* **2013**, *533*, 88.

[30] S. Mueller, J. Muller, U. Schroeder, T. Mikolajick, *IEEE Trans. Device Mater. Reliab.* **2013**, *13*, 93.

[31] M. Masuduzzaman, D. Varghese, J. A. Rodriguez, S. Krishnan, M. A. Alam, *IEEE Trans. Electron Devices* **2014**, *61*, 3490.

[32] X. J. Lou, *Appl. Phys. Lett.* **2009**, *94*, 072901.

[33] T. S. Böscke, S. Teichert, D. Bräuhaus, J. Müller, U. Schröder, U. Böttger, T. Mikolajick, *Appl. Phys. Lett.* **2011**, *99*, 112904.

[34] D. M. Hausmann, R. G. Gordon, *J. Cryst. Growth* **2003**, *249*, 251.

[35] D.-Y. Cho, H. S. Jung, I.-H. Yu, J. H. Yoon, H. K. Kim, S. Y. Lee, S. H. Jeon, S. Han, J. H. Kim, T. J. Park, B.-G. Park, C. S. Hwang, *Chem. Mater.* **2012**, *24*, 3534.

[36] Y. H. Lee, H. J. Kim, T. Moon, K. D. Kim, S. D. Hyun, H. W. Park, Y. B. Lee, M. H. Park, C. S. Hwang, *Nanotechnology* **2017**, *28*, 305703.

[37] T. V. Perevalov, V. S. Aliev, V. A. Gritsenko, A. A. Saraev, V. V. Kaichev, *Microelectron. Eng.* **2013**, *109*, 21.

[38] M. Sowinska, T. Bertaud, D. Walczyk, S. Thiess, M. A. Schubert, M. Lukosius, W. Drube, C. Walczyk, T. Schroeder, *Appl. Phys. Lett.* **2012**, *100*, 233509.

[39] K. S. Jeong, J. Song, D. Lim, M. S. Lee, H. Kim, M.-H. Cho, *Appl. Surf. Sci.* **2014**, *320*, 128.

[40] W. Ostwald, *Z. Für Phys. Chem.* **1897**, *22U*.

[41] R. Materlik, *Dissertation*; University of Applied Sciences Munich, 2018.

[42] M. H. Park, Y. H. Lee, T. Mikolajick, U. Schroeder, C. S. Hwang, *Adv. Electron. Mater.* **2018**, 1800522.

Supplemental Material

SEM was used to determine the grain size of HfO_2 on top of the bottom TiN electrode on the Si substrate. As explained in the experimental introduction, the complete TiN/HfO_2/TiN stack was annealed at 800°C to form the ferroelectric HfO_2 phase. Here, the anneal after TiN top electrode deposition improves the ferroelectric content in the layer and reduces m-phase portions. [1] To measure the HfO_2 grain size, an SC1 etch is used to remove the TiN top electrode. Figure SI 1 shows the surface after TiN removal with an average grain radius of ~12 nm as determined by Gwyddion software using the implemented watershed method as described elsewhere [2,3] (see also experimental part). ToF-SIMS indicated some residual TiO_x on the surface (not shown). Accordingly, an additional 5% HF etch is performed to remove the thin interfacial TiO_x layer at the interface between TiN and HfO_2. Figure SI 2 depicts a clear polycrystalline grain structure with an average grain size of about ~20 nm. To make sure that this image shows the HfO_2 surface, band contrast images of 10 nm sputtered HfO_2 received from electron backscatter diffraction (EBSD) (Figure SI 3) were evaluated with regard to grain size with the Gwyddion software. Figure SI 4 shows a grain size in the range of 20 nm for PVD HfO_2 films similar to the results as gained by SEM. No major enhancement of the grain radius is visible for higher temperature anneals.

From this analysis, it can be assumed that a metal SC1 etch only removes the TiN and the oxidized portion of the TiN grain at the interface to HfO_2 remains. Grains as detected by SEM indicate the grain size of TiN. Only an additional HF etch can remove this TiO_x layer. Then, the grains size of ~20 nm as determined by SEM is similar to the result by EBSD. This is twice as large as previously reported for HfO_2 ALD films [4] and could be caused by the much lower carbon concentration in PVD as discussed before (Figure SI 4). Despite the larger grains, the 10 nm thick PVD films have no monoclinic phase portion and a high remanent polarization, which suggests that defects like carbon can also impact the phase formation.

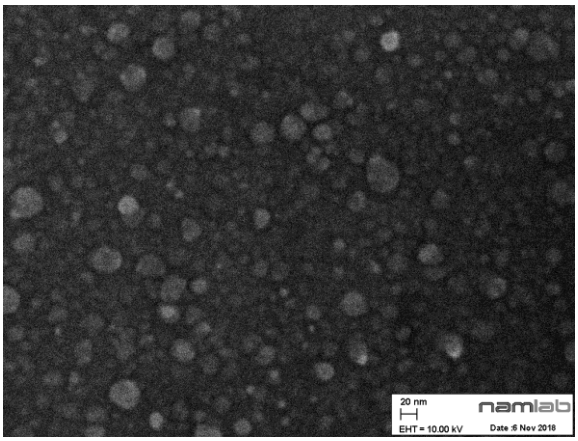

Figure SI 1: SEM of the top surface of a TiN/HfO_2/TiN stack after SC1 etch. The grain radius distribution shows a maximum at ~12 nm indicating TiO_x based remains of the TiN grains.

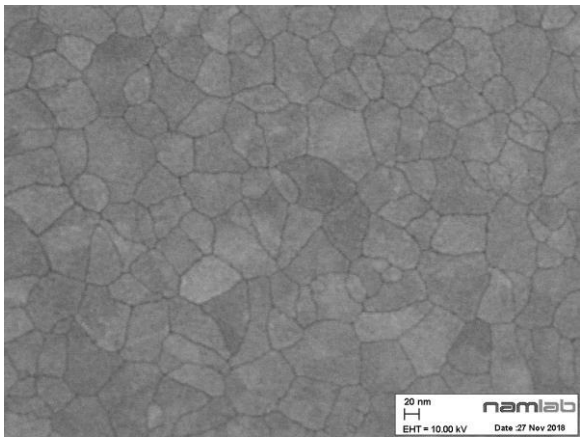

Figure SI 2: SEM image of the top surface of a TiN/HfO_2/TiN stack after SC1 and additional 15 min 5% HF etch. The grain radius distribution shows a maximum at ~20 nm.

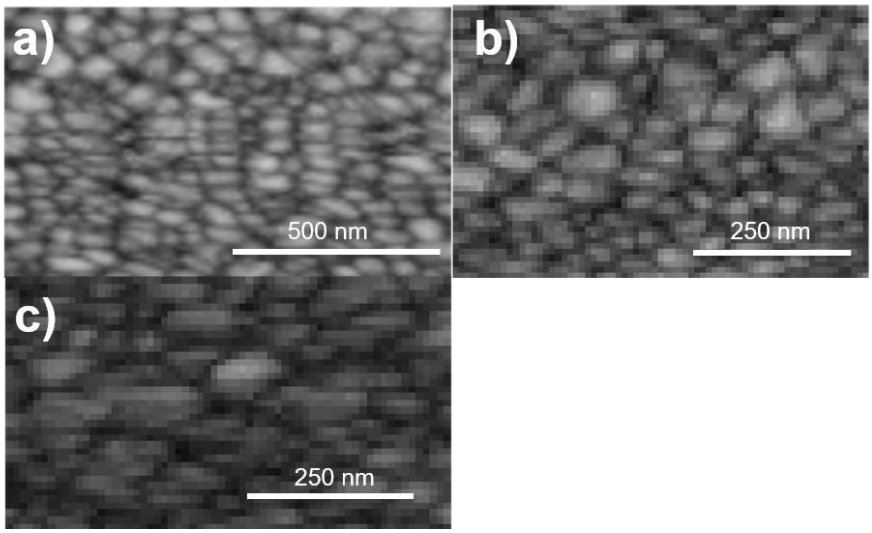

Figure SI 3: Top surface of a TiN/HfO_2/TiN stack after SC1 etch. EBSD Band contrast image of 10 nm sputtered HfO_2 annealed at a) 600 °C, b) 800 °C and c) 1000 °C

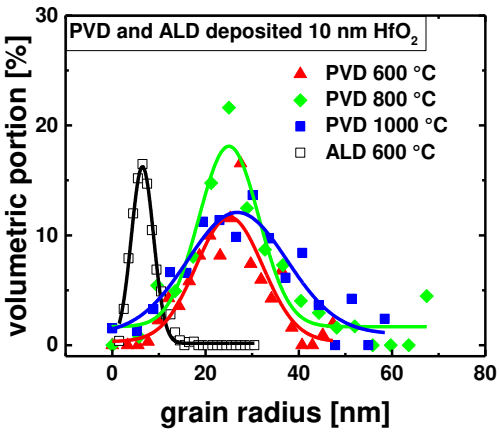

Figure Si 4: Grain size distribution in sputtered HfO_2 at different anneal temperatures compared to an ALD film annealed at 600 °C. The results are obtained from electron backscatter diffraction (ESBD) analyzed with the Gwyddion software and fitted by a Gaussian function.

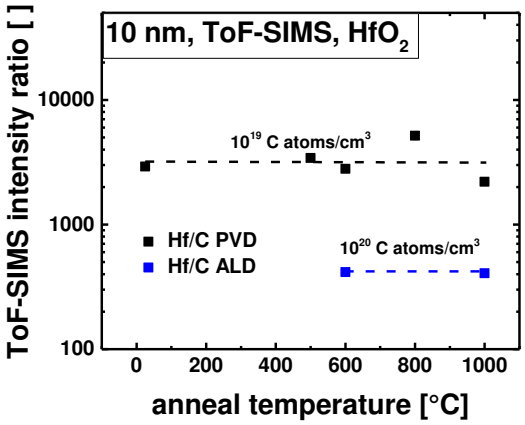

Figure SI 5: Carbon content in HfO_2 films deposited by ALD and PVD measured by ToF-SIMS as a function of anneal temperature.

Carbon content in ALD vs. PVD deposited HfO_2 as determined by ToF-SIMS as a function of annealing temperature (Figure SI 5). A reduction in carbon content by a factor of 10 is visible for PVD films. Furthermore, HAXPES measurements are preformed to determine oxygen vacancy levels in PVD deposited HfO_2 for different O_2 flows.

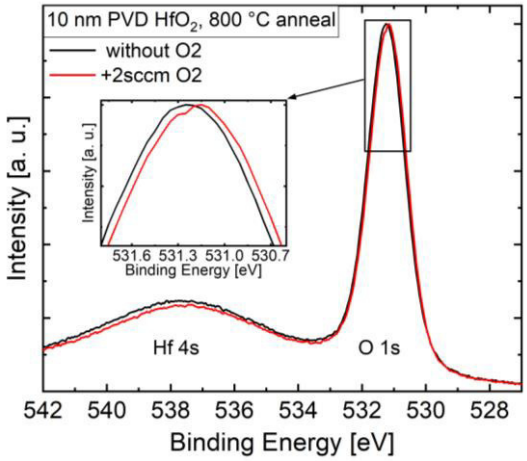

Figure SI 6: Hf 4s and O 1s HAXPES spectra of the samples without additional oxygen and with 2 sccm oxygen flow during the deposition. No O interstitial peak visible at 528 eV after 800 °C anneal.

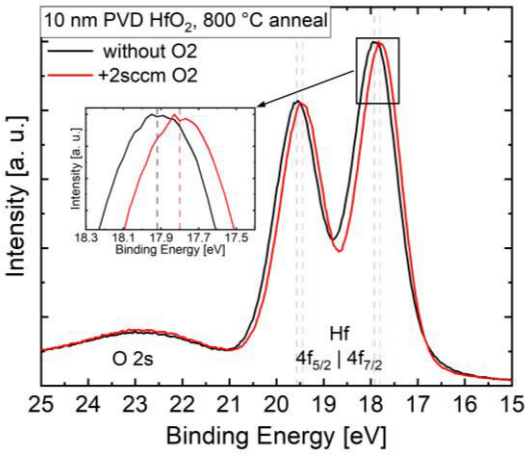

Figure SI 7: Hf 4f HAXPES spectra of the samples without additional oxygen and with 2 sccm oxygen flow during the deposition. Dashed dotted lines highlight the peak shifts.

Similar to figure 7, where GIXRD measurements are performed after different RTP anneals, GIXRD measurements are performed during a slow temperature ramp in nitrogen ambient (figure SI 8). Due to the low temperature ramp rate of 2 K/s, crystallization and phase transitions occur at lower temperatures compared to the results in figure 7 after RTP anneal. Since the sample is purged in an N_2 environment with some residual O_2, an oxidation of the TiN electrode (at 470 °C) and an earlier transformation of the o-phase to m-phase is visible. Overall, phase formation and phase transformations from o- to m-phase are very similar to results reported by Park et al. for doped HfO_2 layers [5] and correlate to DFT calculations for the impact of oxygen in HfO_2 on the phase formation (figure SI 9).[6]

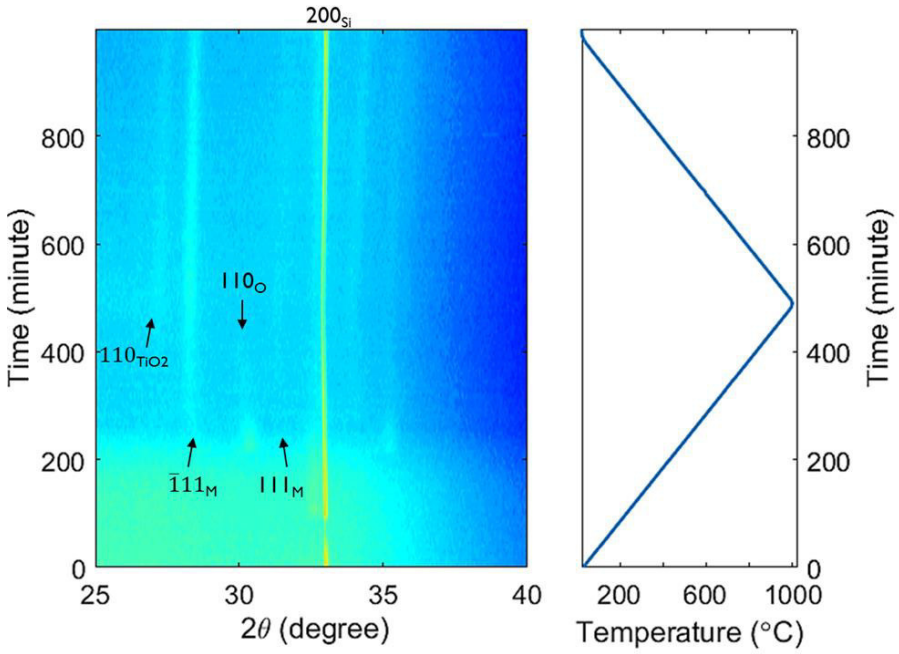

Figure SI 8: Temperature dependent GIXRD of an undoped HfO_2 sample deposited without O_2 flow. Temperature ramp in N_2 ambient with a ramp rate of 2K/s.

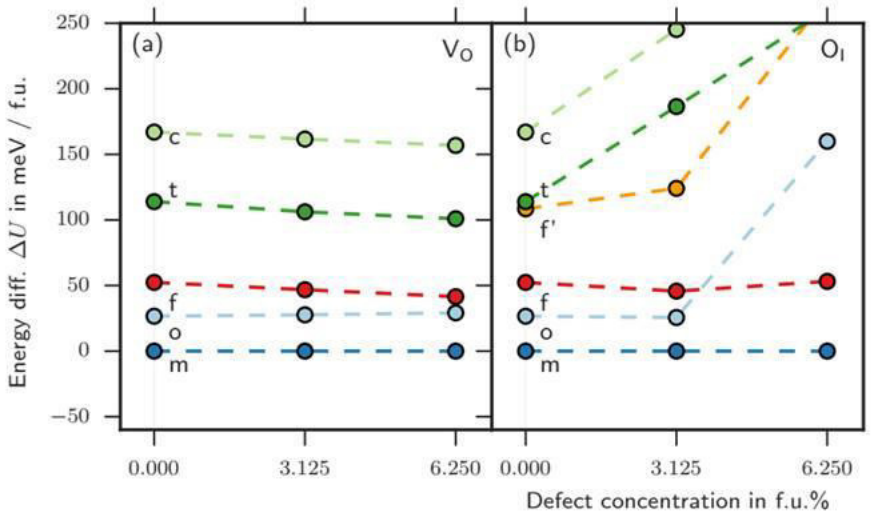

Figure SI 9: Effect of oxygen vacancies (a) and interstitials (b) on the total energy difference ΔU_o of various HfO_2 polymorphs compared to the m-phase [6].

Figure 9 shows the GIXRD pattern of PVD HfO_2 for different O_2 flow after deposition before any further heat treatment. The peak of the o- and m-phase peaks at $2\theta \sim 30°$ are fitted by a Gaussian function (Figure SI 10b) and the determined grain size is plotted as a function of O_2 flow during PVD deposition (Figure SI 10a).

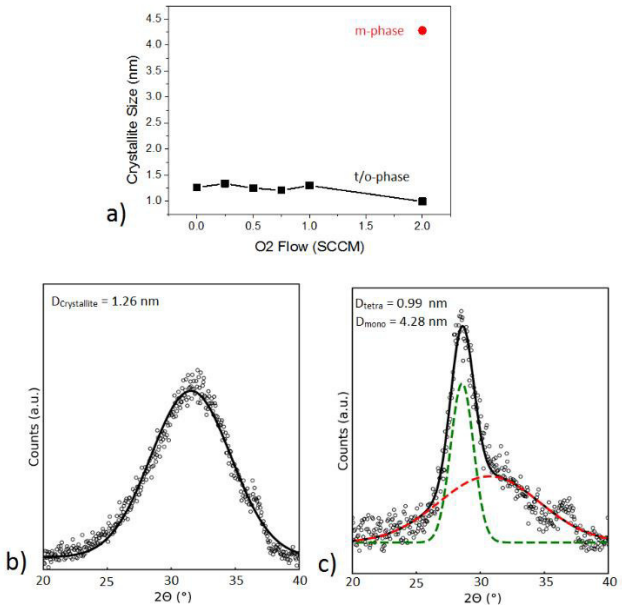

Si Figure 10: Crystallite size of the as-deposited HfO_2 thin films with O_2 flow. Gaussian functions were fitted to the experimental data in Figure 9 to calculate the crystallite size for b) 0 sccm and c) 2 sccm of O_2.

[1] T. S. Böscke, J. Müller, D. Bräuhaus, U. Schröder, U. Böttger, *Appl. Phys. Lett.* **2011**, *99*, 102903.
[2] H. J. Kim, M. H. Park, Y. J. Kim, Y. H. Lee, W. Jeon, T. Gwon, T. Moon, K. D. Kim, C. S. Hwang, *Appl. Phys. Lett.* **2014**, *105*, 192903.
[3] D. Nečas, P. Klapetek, *Open Phys.* **2012**, *10*.
[4] T. Mittmann, F. P. G. Fengler, C. Richter, M. H. Park, T. Mikolajick, U. Schroeder, *Microelectron. Eng.* **2017**, *178*, 48.
[5] M. H. Park, C.-C. Chung, T. Schenk, C. Richter, K. Opsomer, C. Detavernier, C. Adelmann, J. L. Jones, T. Mikolajick, U. Schroeder, *Adv. Electron. Mater.* **2018**, *4*, 1800091.
[6] R. Materlik, *Dissertation*; University of Applied Sciences Munich, 2018.